

# Powder Diffraction from a Continuous Micro-Jet of sub-micron Protein Crystals

D.A. Shapiro<sup>1,4</sup>, D. DePonte<sup>2</sup>, R.B. Doak<sup>2</sup>, P. Fromme<sup>3</sup>, G. Hembree<sup>2</sup>, M. Hunter<sup>3</sup>, S. Marchesini<sup>1,4</sup>, K. Schmidt<sup>2</sup>, D. Starodub<sup>2</sup>, U. Weierstall<sup>2</sup>, H. Chapman<sup>5</sup>, J. Spence<sup>2</sup>

<sup>1</sup> Advanced Light Source, Lawrence Berkeley National Laboratory, 1 Cyclotron Road, Berkeley, CA 94720, USA

<sup>2</sup> Department of Physics, Arizona State University, Tempe, AZ 85287, USA

<sup>3</sup> Department of Chemistry and Biochemistry, Arizona State University, Tempe, AZ 85287, USA

<sup>4</sup> Center For Biophotonics Science and Technology

<sup>5</sup> Deutsches Elektronen- Synchrotron, DESY, Notkestraße 85, D-22607 Hamburg, Germany.

## Abstract

Powder diffraction rings have been obtained from sub-micron protein crystallites in a water jet, and the data analysed. Previous powder diffraction has used a suspension of small crystallites, and long exposures, causing significant X-ray damage. We show here that protein powder data from nano-crystals can be obtained using a continuous micro-jet. This allows more efficient use of crystal growth solutions containing nanocrystals and the much shorter exposures needed for next-generation synchrotrons. This method requires neither the crushing of larger polycrystalline samples nor any techniques to avoid radiation damage such as cryo-cooling. We have commissioned an apparatus to record protein powder diffraction in this manner and in this paper present the first such patterns from photosystem I protein crystals with sizes less than 500 nm. These preliminary patterns show the lowest order reflections, which agree quantitatively with theoretical calculations of the powder profile. The results serve also to test our aerojet injector system, with future application to femtosecond diffraction in Free Electron X-ray Laser schemes, and for Serial Crystallography, using a single-file beam of aligned hydrated molecules. For this purpose filtration allows continuous particle size reduction to the single molecule level.

## Introduction

The major bottleneck in protein structure determination by x-ray diffraction from single crystals is the production of high quality crystals that are large enough for diffraction analysis. Protein crystallography beamlines that utilize third generation synchrotron sources typically require crystals that are at least 100 microns in size for the collection of atomic resolution data. The size of the crystals required for data collection increases with the size of the unit cell. As an example, crystals larger than 500 $\mu$ m were essential for the structure determination of Photosystem I at 2.5 Å resolution (Jordan, 2001). Photosystem I is a membrane protein with a molecular weight of 1 056 000 Da and represents one example of a class of proteins that are difficult to crystallize. The production of large well ordered single crystals of difficult to crystallize proteins can take years and may involve very time consuming investigations like the determination of phase diagrams or seeding techniques. Even micro-diffraction probes are limited to crystals several tens of microns in size, but high X-ray exposure of small single crystals can lead to a severe problem of radiation

damage. Most membrane protein crystals suffer from X-ray damage during X-ray data collection even at cryogenic temperatures. Small single crystals of membrane proteins fail to show high resolution diffraction after seconds of exposure, so that when using small micron-size crystals, hundreds of partial data sets may be needed. That method has been used to determine the first high resolution structure of a G-protein coupled receptor (Rasmussen et al., 2007), a class of membrane proteins that represent more than 50% of all current drug targets. Alternatively, data collection has to be performed using large single crystals that can be shifted to new areas several times during data collection to limit damage .

At the same time, optical microscopy evidence suggests that many crystallization solutions may contain large numbers of small crystals of the size of about one micron or smaller (Von Driel, 2007), and that the mother liquor in crystal growth wells contains a high concentration of these nuclei. Experiment and theory indicate that such small crystals do not contain enough molecules for statistically significant scattering prior to destruction of high-resolution detail by radiation damage. The smallest protein crystals in common use are now about 10-30 microns, large enough to handle and mount on a goniometer. These considerations have led to a revival of interest in powder protein crystallography (Margiolaki and Wright (2007).

In this paper we report preliminary results from a serial protein crystallography project that aims to provide a proof of concept that X-ray diffraction can be detected from a stream of droplets that contains nano-crystals. As the model protein we did not choose lysozyme, but Photosystem I, which is the largest and most complex membrane protein that has been crystallized to date. The central component of this method is a single-file droplet beam, containing nanocrystals, which originates from a Gas Dynamic Virtual Nozzle (aerojet) (DePonte et al 2008, Weierstall et al 2008) droplet source and traverses a quasi-continuous x-ray beam. The jet, which can be driven by a syringe pump or high-pressure gas, may be filled directly with mother liquor from crystal growth cells, allowing us both to test the jet and evaluate the prospects for using it for powder protein diffraction. The aerojet design uses gas to focus a small jet from a bigger nozzle large enough to avoid clogging. The current data are limited in resolution only by the long wavelength of the soft X-rays. The method also shows potential for high throughput screening of crystallization drops for microcrystals. Since the droplets are moving with a velocity of the order of 10 m/s and the x-ray beam is only a few tens of microns wide each protein nanocrystal is exposed to x-rays for only 2 microseconds and thus is not damaged by the ionizing radiation. Using tabulated data for elemental photoabsorption cross sections (Henke et al 1993), we obtain a mass absorption coefficient  $\mu = 6.1 \times 10^4 \text{ cm}^2 \text{ g}^{-1}$  at an X-ray energy  $E = 530 \text{ eV}$  for a generic protein stoichiometry  $\text{H}_{50}\text{C}_{30}\text{N}_9\text{O}_{10}\text{S}_1$ . The energy per unit mass (dose) deposited into a protein nano-crystallite during its passage through the X-ray beam can be estimated as  $D = \mu E I_0 t = 1.3 \times 10^3 \text{ Gy}$ , where  $I_0$  is the incident X-ray flux (number of photons incident per unit area per unit time. Measurements of Bragg reflection fading at prolonged exposure for a ribosome crystal (Howells et al, 2008) suggest that the maximum tolerable dose without observable damage at a resolution of 10 nm for our experimental arrangement is  $10^9 \text{ Gy}$ . Note that the (200) reflection of the photosystem I crystals corresponds to the interplanar distance of 12.2 nm. In another work, no change at a resolution of 18 nm was observed in a frozen-hydrated yeast cell for a dose of  $5 \times 10^9 \text{ Gy}$  (Shapiro et al 2005). Thus, the radiation damage threshold far exceeds the dose received by each crystallite in our experiments. The detector integrates the diffracted intensity as the droplets are continuously refreshed by the aerojet source. Large total exposure times are therefore available without damaging the

crystallites. The effective exposure time is calculated from the incident intensity and the number of proteins simultaneously exposed.

Eliminating the necessity for large crystal sizes allows the possibility of obtaining structural information from single crystals or even single oriented molecules. Therefore, the new method has also a very high potential for the structure determination of X-ray structures using a stream of microcrystals synchronized with an X-ray laser or -in the long term- even the structure determination using a stream of oriented single hydrated protein molecules, which would allow the study of the patterns in the transition to the "gas phase" diffraction, where particle-size line-broadening prevents identification of the reciprocal lattice, and external molecular alignment is required. Detailed calculations for GroEL (Starodub et al 2008) indicated that 7 Angstrom resolution, sufficient for seeing secondary protein structure, is obtainable at current synchrotron sources if only one aligned protein is present in the x-ray beam at any instant. Several approaches to the problem of aligning the proteins have been discussed, including use of the dipole moment induced by a powerful CW laser (Spence and Doak, 2004), flow alignment, and static magnetic or electric fields, of which the first two are under development in our laboratory. Molecular alignment under converging and extensional flow conditions studied by SAXS has been demonstrated elsewhere (Kisilak et al 2001), as has laser-alignment of beams of organic molecules probed by X-ray absorption spectroscopy (Peterson et al 2008).

Pending final development of alignment methods for serial crystallography, we show here that X-ray diffraction data may be obtained using our aerojet of small protein crystals without alignment, by applying the methods of powder diffraction to sub-micron crystallites within the droplets. Since the dimensions and symmetry of the unit cell can be determined from the ring pattern, powder diffraction avoids the need to solve the molecular alignment problem. Ultimately this is traceable to the fact that, because there is limited number of ways to arrange points periodically in space with identical environments, there is a finite number of Bravais lattices, over which an exhaustive search is possible. There is no such constraint for a single molecule.

We demonstrate for the first time solution x-ray scattering from a micro-jet of hydrated nano-scale crystals. Experiments were carried out using 530 eV x-rays with both 50 nm gold nanospheres and crystals of the membrane protein Photosystem-1 with sizes of less than 500 nm. The use of such long wavelengths, particularly in the water window, increases the scattering cross-section (thereby decreasing exposure times and particle concentrations needed) and reduces the effects of solution scattering. Gold spheres were used as a test object to optimize nozzle performance and data acquisition/analysis techniques. A theoretical simulation of the experiment fits the gold diffraction pattern and provides structural information that closely agrees with the manufacturer's analysis. The protein crystals were size restricted with a nano-porous filter to sizes of 500 nm. Our preliminary experimental geometry and the long wavelength of the soft X-rays only allows for the observation of the lowest order diffraction rings but our results closely match theoretical predictions from the known structure.

## **1. Experimental**

Diffraction data were collected at beamline 9.0.1 of the Advanced Light Source where the beam defining optics are optimized for coherent soft x-ray scattering experiments (Figure 1). The source, a 10 cm period undulator with 43 periods, provides 530 eV photons in the third harmonic with an approximate photon flux of  $10^{12}$  photons/second in a 50 micron focus provided by a monochromatizing zone plate segment. The combination of a nickel coated relay mirror and beryllium vacuum window act as a bandpass filter that removes higher and lower undulator

harmonics while the remaining undulator spectrum is dispersed vertically by the off-axis zone plate segment. This 550 micron diameter zone plate segment focuses the third undulator harmonic to a 50 micron spot one inch upstream of the droplet beam. This spot is then selected with a 50 micron pinhole. Experiments requiring greater transverse and longitudinal coherence use smaller beam defining pinholes so that fewer coherent modes may be selected. Accepting the full undulator harmonic results in a bandwidth equal to the source bandwidth that is approximately equal to  $1/mN$  where  $m$  is the harmonic number and  $N$  is the number of undulator periods. This neglects electron beam size and divergence and for our case provides an upper limit on the bandwidth of 0.8%, though the actual value will not be significantly different.

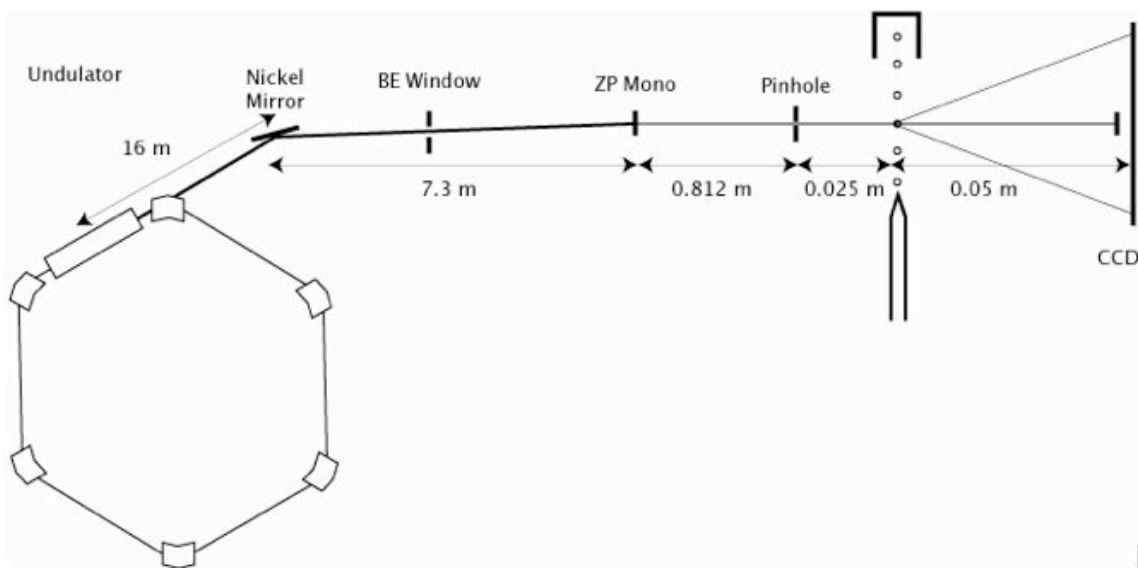


**Figure 1** Beamline layout. The monochromator focuses the undulator beam in the vicinity of the droplet source for maximum photon flux and the 1 square inch detector is located 5-10 cm downstream. An upgrade currently underway replaces the nickel mirror with a multilayer mirror allowing operation at up to 1500 eV.

Focusing of the x-ray beam is essential because of the flux-limited nature of this experiment. The beam divergence, dominated by the zone plate focusing with focal length of 80 cm and the large x-ray bandwidth, result in significant angular broadening of the scattered peaks. An undulator source at the ALS has a central cone divergence of approximately 40  $\mu$ rad, which is at least a factor of 20 smaller than the other sources of beam spread. At the largest scattering angles recorded (12 degrees) the angular width of a scattered beam is at least 0.13 degrees though the precise value is not known without a quantitative measurement of the x-ray monochromaticity. The detector used, a Princeton Instruments MTE2-1300B CCD, has sufficient angular resolution to make accurate measures of the powder peak profiles. The 20 micron pixels, at a 9 cm working distance, provide an angular resolution of 0.01 degrees or 11.5 detector pixels per peak FWHM. In light of this, the detector was binned by a factor of four in each dimension for faster readout.

The particles of interest are delivered to the x-ray beam in a continuous liquid jet which breaks into droplets further downstream due to a Rayleigh necking instability (Rayleigh (1878)). The jet, which is described in detail elsewhere (Weierstall et al, 2008), consists of a column of particle-containing solution which flows through a 50 micron inner-diameter hollow tube (fiber optic) and is accelerated upon exiting the tube by a coaxial flow of carbon dioxide gas into vacuum. The CO<sub>2</sub>, which acts to focus the liquid stream, condenses as dry ice on a liquid-nitrogen cooled coldtrap, thereby minimizing the rise in pressure caused by the liquid and gas leak into the vacuum chamber. The acceleration by co-flowing gas thus serves the purpose of reducing the jet diameter, allowing use of a larger nozzle, which is less likely to clog. A typical jet diameter for the images shown here was 10 microns, which corresponds to a flow rate of a few tens of micro-liters per minute. Figure 2 shows a liquid jet emerging from the nozzle exit averaged over an exposure time of 1 second, while figures 3(A) and 3(B) show flash (nanosecond) images of the droplets some greater distance from the nozzle tip. In figure 3(B), we have controlled the droplet generation rate using a piezo-electric actuator, which may be synchronized to a pulsed X-ray source for experiments aimed at reading out the diffraction pattern from single molecules, using a very fast read-out area detector (Neutze et al (2000), Ourmazd et al (2008)). However, for the results reported here, the droplet breakup was un-triggered and occurred with the intrinsic Rayleigh instability frequency.

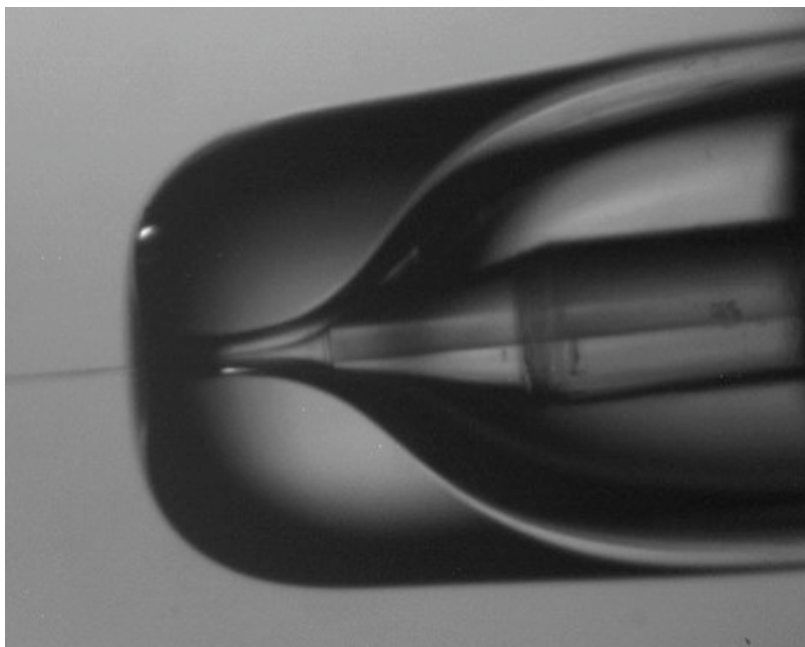


**Figure 2** Aerojet droplet source. An inner capillary, a hollow fiber-optic with 50 micron inner diameter, carries the particle solution which is pressurized to 150 PSI. The outer glass capillary carries the focusing CO<sub>2</sub> gas at 15 PSI, which expands into vacuum producing a small jet of solution that breaks up into droplets.

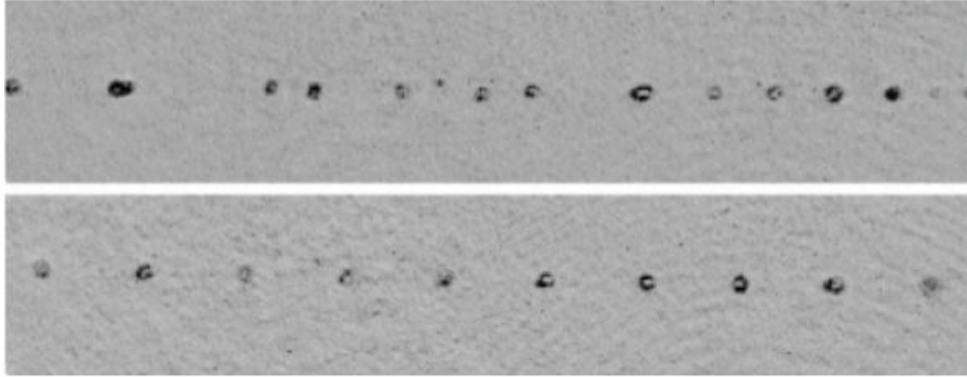


**Figure 3** Flash image of the aerojet droplets (exposure time 100nsec). (A) Untriggered droplets are unevenly spaced and have a distribution of sizes. (B) Triggered droplets are evenly spaced and have a much narrower size distribution.

## 2. Data and Analysis

Completed one-dimensional datasets are reduced from dozens of individual two-dimensional CCD recordings. The dynamic range of the CCD is significantly lower than that of the diffraction patterns so data must be collected on multiple time scales and then stitched together during post-processing. Furthermore, taking multiple CCD recordings for each exposure time and then averaging the results improves statistics. The centers of the diffraction patterns are found experimentally by attenuating the incident beam and then taking a direct measurement of its position on the CCD. This position can then be fine tuned to sub-pixel resolution by calculating the center of mass of the scattering pattern. During normal data acquisition the direct beam is not attenuated and must be blocked by a beamstop in order to avoid damaging the sensitive detector, and therefore the data at very small scattering angles is lost. The center position is then used for a radial averaging procedure that produces the final dataset from the assembled two-dimensional diffraction patterns.

Scattering from the solution in which the particles are embedded leads to a background signal. The strongest contribution to the diffraction pattern from the solution results from total external reflection at the solution's surface. The proximity of the nozzle tip to the x-ray beam can be adjusted so that various points along the jet path can be probed. Diffraction patterns from the continuous jet immediately adjacent to the tip (a continuous column of liquid) show a sharp vertical streak due to x-rays scattered from the horizontal jet's surface. X-rays scattered from the solution's interior are detected in all scattering directions and are significantly weaker. If instead, the droplet region of the jet is probed, then the surface scattering is also isotropic, producing a disk of scattering reflected from a thin band around each droplet at the specular external reflection condition. The cutoff radius of this diffraction disk is set by the critical angle for external reflection. At higher beam energies, this cutoff and the disk diameter shrink rapidly. At our low energy, the disk greatly decreases the signal-to-noise ratio since it is only particle scatter that we are interested in. For this reason, all experiments were carried out using the continuous jet.

### a. Gold Nano-spheres

Initial experiments were performed using gold nano-spheres as test objects to verify the integrity of the structural information obtained by this technique. The spheres (Ted Pella, part no.EM.GC50) were 52 nm in diameter and had a concentration of  $4.5 \times 10^{10}$  particles per mL. A flow rate of 30  $\mu\text{L}/\text{minute}$  implies  $2.3 \times 10^7$  balls per second passed through the x-ray beam. Assuming a liquid flow speed of 10m/s and a 50 micron wide X-Ray beam, this indicates that 120 gold balls were continuously present in the beam at any instant. The motion of the balls does not affect the far-field diffraction pattern because the binned CCD pixels are larger than the x-ray beam diameter; therefore the exposure time is identical to that for 120 stationary balls. (Similar considerations also apply to proteins, which, because they are continually refreshed, avoid damage). This number indicates that the droplet source is a sample with sufficient strength to be readily measured with our available flux. Indeed, the maximum exposure time used in this experiment was 1.5 seconds and provided scattered intensity to the edge of our detector. The total exposure after averaging was about 30 seconds. It is worth noting that the exposure time of any single gold ball in the sample was only 5 microseconds.

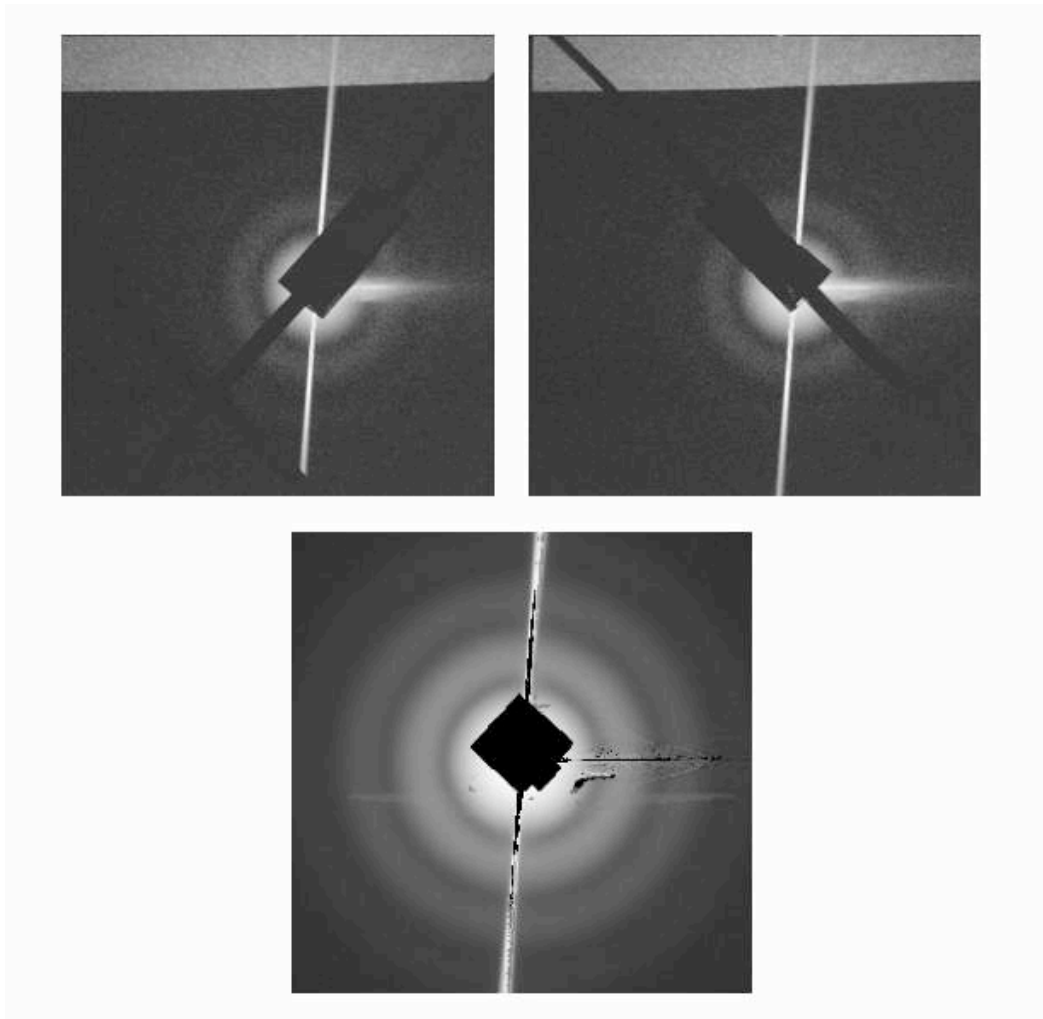
Figure 4 describes the data reduction process. The system was designed with the intention of collecting diffraction patterns from streams of aligned particles (Spence and Doak, 2004). In the case of aligned particles it is necessary to record intensities on the 2D detector at all points around the incident beam. Thus, the beamstop was designed to provide this functionality through the acquisition of two separate patterns at different beamstop positions. The shadow of the beamstop is rotated by 90 degrees between the two positions and when merged leave only a square of missing data at the very center of the diffraction pattern. Diffraction data are collected with the droplet beam on and with the droplet beam off for background subtraction. The pixels in the areas of very high noise, near nozzle tip scatter and jet scatter, are not reliable and so are masked before calculating the radial average.

The use of very long wavelengths and large scattering angles means that Ewald sphere curvature effects will be present in the recorded diffraction patterns. The spatial frequencies recorded lie on a sphere in reciprocal space that is described by:

$$q_z = \frac{1}{\lambda} - \sqrt{\frac{1}{\lambda^2} - q_y^2 - q_x^2}.$$

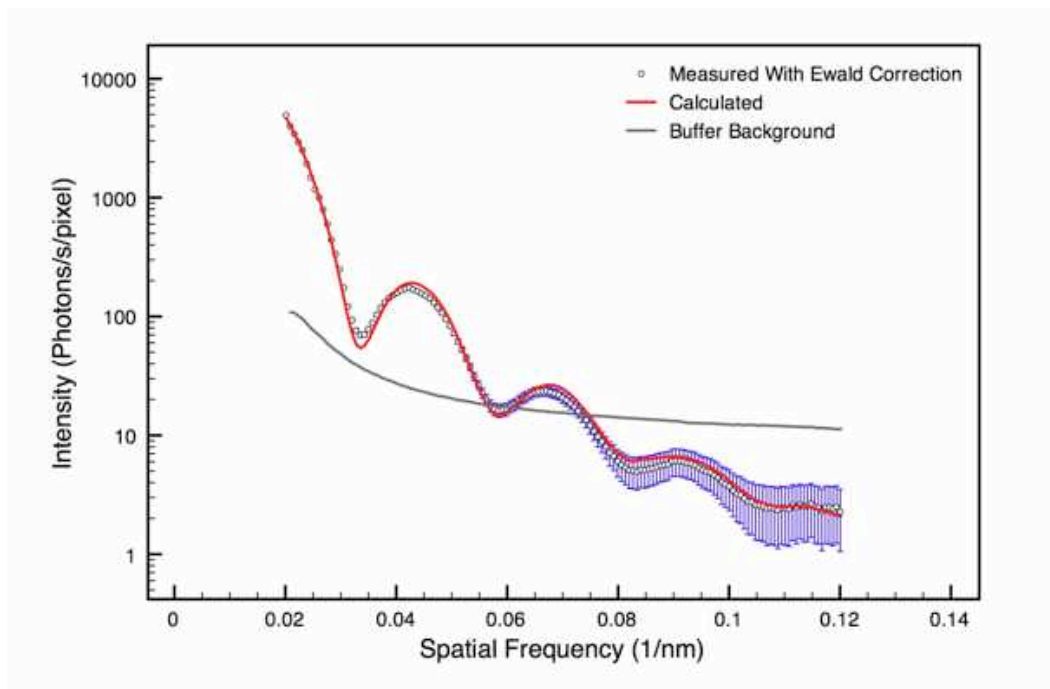
Since the scattered intensities are recorded on a plane they represent a gnomonic projection of the Ewald sphere and are offset radially by a distance in q-space that increases with scattering angle. This offset is given approximately by  $\lambda^2 q^3 / 2$  where  $q = \sqrt{q_x^2 + q_y^2}$  is in the detector plane.

Figure 5 shows the result of radially averaging the final pattern in figure 4 where the spatial frequencies indicated on the horizontal axis have been corrected for Ewald sphere curvature. The solid curve is a simulated diffraction pattern calculated from an ensemble of gold spheres with normally distributed diameters centered on 50.3 nm and a standard deviation of about 3.8 nm. The manufacturer of the particles (Ted Pella Inc., [www.tedpella.com](http://www.tedpella.com)) claims a coefficient of variation of <8%, which is in close agreement with our analysis.



**Figure 4** Assembly of two dimensional diffraction patterns. Full datasets are collected by the use of two beamstops that are oriented at 90 degrees to each other. The vertical streaks are x-ray scatter from the continuous column of liquid leaving the nozzle gas aperture. Photons detected outside of those streaks originate from the particles within the buffer solution. Photons scattered off the nozzle tip form a bright horizontal streak to the right of the beamstop. Many patterns are averaged and data from opposing beamstops are merged to give the final dataset at bottom. This process is not necessary for particles with isotropic scattering patterns but becomes essential if the particles scatter non isotropic and are aligned.





**Figure 5** Radial average of Figure 3. The circles are experimental data after background subtraction and the continuous red curve is calculated from a simulated diffraction pattern. The simulation represents an ensemble of gold spheres with normally distributed diameters with central diameter of 50.3 nm and standard deviation of 3.8 nm. This is in close agreement with the manufacturer's analysis, which claims 8% coefficient of variation. The solid grey curve shows the scattering pattern from a gold buffer solution for gold spheres that was subtracted as background from the gold particle pattern.

### **b. Photosystem-1 Protein Nano-crystals**

Photosystem I crystal samples were prepared from the cyanobacterium *Thermosynechococcus elongatus* as described elsewhere (Jordan et al (2001)). Briefly, the cells were grown under low-light conditions to allow for a high yield of trimeric photosystem I. The cells were harvested, lysed, and the proteins extracted with detergent (beta-dodecylmaltoside) and isolated using an anion-exchange chromatography. with eluent solutions composed of 20 mM MES pH 6.4, 0.02% (m/v) (beta-dodecyl maltoside), and a MgSO<sub>4</sub> gradient was used for the elution of the protein. After purification, the photosystem I was diluted to low-salt conditions (final concentration 20 mM MES pH 6.4, 6 mM MgSO<sub>4</sub> and 0.02% (m/v) beta-dodecyl maltoside, which leads to the growth of micron and submicron sized crystals spontaneously over night at 4°C..

The size of the PS1 crystallites was then restricted by placing a 500 nm filter in the liquid line of the aerojet. With many such crystallites per droplet, the recorded diffraction pattern contains contributions from crystallites in all possible orientations. This generates a sphere centered on the origin of reciprocal space for every reciprocal lattice point, which is intersected on a circle by the Ewald sphere, producing the familiar Debye-Scherrer diffraction rings. In reality, this sphere

is a shell of finite thickness, which depends on several experimental factors. These include beam divergence, spectral bandwidth, crystallinity effects such as imperfections or finite crystal size, and also instrumental broadening resulting from finite angular resolution. Fig. 6 shows powder diffraction peaks corresponding to (010), (011) and (020) reflections. The (011) peak at 9.9° overlaps with the (110) peak at 9.6°. The latter is manifested by a small asymmetric left shoulder and constitutes 2% of the peak area. As noted earlier, the peak width due to the characteristics of the x-ray illumination is 0.13 degrees. In figure 6, the measured powder peaks have FWHM widths of about 0.25 degrees. The additional peak width must therefore result from crystallinity and finite size effects. If the small crystallites are coherently illuminated then the Bragg peaks will be convolved with the diffuse coherent scatter that represents the overall crystal morphology. Averaging this effect over many such crystals will give a broadened powder profile whose width is inversely proportional to the average crystal size. The number of coherent modes in our beam is given approximately by

$$N = 2 \frac{x \cdot x'}{\lambda}$$

where  $x$  is the beam size in the monochromator focus and  $x'$  is the beam divergence. This gives 27 coherent modes in our 50 micron beam or about 2 microns per mode. Thus, all of the crystallites are coherently illuminated and it is not likely that neighboring crystals interfere coherently. The average crystal size associated with our observed angular spread is  $d = \lambda/\theta = 585$  nm and corresponds to PS-I crystals with 19x19x32 unit cells, or about 23,000 molecules per crystal. Each unit cell consists of two trimers. The crystallites form hexagonal needles with an aspect ratio of between 5 and 10. The spacegroup is  $P6_3$ , and the molecular weight is 1056000 Da. The Photosystem I crystals have a solvent content of 80%: the mean electron density within the unit cell is 667 e/nm<sup>3</sup>, and the hexagonal unit cell dimensions are  $a = b = 28.8$ nm (288 Å),  $c = 16.7$ nm (167 Å). It is remarkable that strong powder diffraction rings have been detected with this small number of molecules/crystal and the extremely short exposure time/droplet. The exposure time for the diffraction pattern was only 30s, with a flow rate of 10µl/s, i.e. only very small amounts of samples (5µl) have been used for the diffraction pattern. This small sample volume would allow the development of the use of the droplet stream for the high-throughput robotic screening of crystallization drops for microcrystals that not visible by optical microscopy.

The projection of three-dimensional data onto one dimension in powder diffraction results in a loss of information in two ways (see David et al (2002) for a review). Firstly, at large angles the decreasing ring spacing eventually becomes less than the angular resolution of the instrument, setting a limit on the ultimate resolution of the density map. Secondly, overlaps can occur in space-groups of higher symmetry than orthorhombic due to indexing accidents, so that structure factors of different magnitude contribute to the same ring. Degeneracies due to point, space-group and chiral symmetries may also be masked, and these must be known to extract structure factor magnitudes unless, as in the charge-flipping method, the analysis is always performed in P1. In a previous paper (Wu et al (2006)), we have shown how a variant of this charge-flipping algorithm can resolve both the accidental degeneracies and the symmetry degeneracy in powder data from inorganic crystals. The most common space group for proteins is orthorhombic  $P2_12_12_1$ , which has no accidental overlaps. Experimental powder patterns have recently been obtained from hen egg-white lysozyme that extend to 2 Angstroms [11], and the structure has been determined using the molecular replacement for the phase determination (Von Dreele,

2007). For a sufficiently low-symmetry space group in which each ring corresponds to a different structure factor magnitude, given that the Bravais lattice has been determined from the ring spacings, one may in principle be able to assign structure factor magnitudes to points on the three-dimensional reciprocal lattice, and so use any existing single-crystal method to phase and invert the data. Practical considerations limit the potential of powder diffraction for protein structure determination and a considerable literature has been devoted to the problem of resolving peak overlaps using techniques developed by Reitvelt, Le Bail and Pawley (David et al (2002)). This problem might be solved in the future for peak overlaps of small proteins, but deconvolution of high resolution powder diffraction of crystals of large proteins like photosystem I might be very difficult- if not impossible. However, low resolution data could provide valuable information about the molecular envelope and the oligomeric state of large multi-protein complexes. Our flipping method (Wu et al (2006)) extends the iterative Le Bail method to complex quantities in the framework of the Fienup iterative algorithms. Reitvelt refinement requires a structural model and so can only be used for phase determination of proteins, for which a homologous structure is already available, while the iterative Le Bail and Charge Flipping methods do not, but may require atomic resolution data. Research aimed at obtaining a low-resolution envelope from powder data which does not extend to atomic resolution using iterative techniques is in progress. In a recent paper we have shown that the powerful charge-flipping method is a special case of the Fienup Output-Output algorithm (Wu et al (2004)).

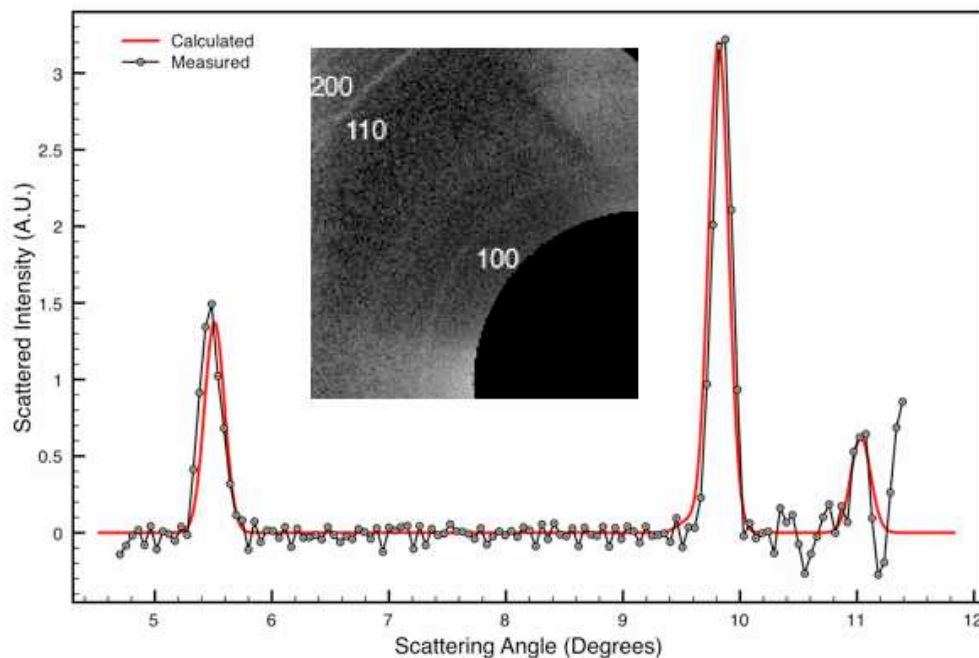


**Figure 6** Powder pattern from photosystem-1 nano-crystals with sizes less than 500 nm. The measured  $q$ -vectors have Miller indices of 100, 110, and 200. The solid red curve represents a calculated powder pattern and is in good agreement with experiment. The inset shows a subset of the experimental data with background subtracted.

The density of reciprocal lattice points for a triclinic crystal may be found as a function of scattering angle  $\Theta = \lambda/d$  (twice the Bragg angle  $\Theta_B$ ) as (David et al (2002)),

$$\frac{\Delta N}{\Delta \theta} = \frac{\pi^2 \sin\left(\frac{\theta}{2}\right) \sin(\theta)}{45\lambda^3}$$

Thus peak density is proportional to the square of the scattering angle for small angles, inversely proportional to  $d^2$  (for  $d < \lambda$ ), proportional to cell volume, and inversely proportional to  $\lambda^3$ . This function has a maximum at  $\Theta_B = 2 \tan^{-1}(\sqrt{2}) = 109^\circ$ , where  $\Delta N \approx V/20$  per degree for hard X-rays around  $d = 1 \text{ \AA}$ . Our use of long wavelength (2.3 nm) thus greatly improves peak separation, while limiting ultimate resolution (an upgrade to 3 kV is planned, allowing 7 Angstrom resolution). We use an undulator insertion device for high flux (focused to the 20 micron diameter of our droplet beam), and take advantage of the  $\lambda^4$  dependence of coherent scattered intensity (Howells et al (2008)). This enables short exposure times from our droplets, which contain relatively few protein molecules. Much longer exposure times would be necessary using Angstrom wavelengths at bending-magnet synchrotron sources.

#### 4. Conclusion

We have demonstrated for the first time solution x-ray scattering from a micro-jet of nano-scale crystallites of a membrane protein using a synchrotron undulator source. For un-crystallized particles, this procedure yields the equivalent of a small-angle x-ray scattering (SAXS) pattern while for small crystallites it yields a powder diffraction profile. Our analysis shows that quantitative structural information may be obtained from the scattering data acquired in this manner. The primary benefit of this technique is that the smallest available protein crystals may be used without any concern for radiation damage. When combined with the new iterative phasing methods, this approach may provide low-resolution molecular envelopes from protein nanocrystals. Currently, there is no other x-ray scattering technique that can utilize such small crystals with such ease. Furthermore, shorter wavelengths and the possible use of particle alignment schemes, currently under development, may allow for the *ab initio* phasing of these diffraction patterns and provide structural maps in the several angstrom range. The incident flux density required for x-ray imaging is inversely proportion to  $\lambda^2$  while the dose (energy deposited/mass) is relatively independent of energy from 1-10 keV. This seems to indicate that the lowest energies compatible with the desired resolution should be used. Recent theoretical simulations show that 7 Å resolution should be obtainable using planned undulator sources with energies of around 3 keV.

The aerojet droplet source, being a very high brightness particle beam, is also ideally suited for experiments with pulsed x-ray sources. The triggered droplet beam may be precisely synchronized to the x-ray pulses so that all proteins are utilized. This is in contrast to electro-spray injection schemes that produce a highly divergent particle beam and cannot be synchronized. Furthermore, the remaining water layer surrounding the proteins may be continuously adjusted by altering the transit time, i.e. evaporation time, between droplet source and x-ray beam. It has been suggested that this water layer may act as a tamper to slow the explosion of proteins in such intense x-ray pulses and allow the use of longer pulses for the

acquisition of atomic resolution diffraction data. Finally, this aerogel device produces a stream of uncharged particles and thereby eliminates possible damage to the molecules associated with the high molecular charge as observed in electrospray mass spectroscopy.

### **Acknowledgements**

We graciously acknowledge support from the staff of the Advanced Light Source at Lawrence Berkeley National Laboratory. This research is supported by grants from The Center for Biophotonics Science and Technology at the University of California at Davis, the National Science Foundation (IDBR-0555845) and ARO (W911NF-05-1-0152). The Advanced Light Source at Lawrence Berkeley National Laboratory is supported by the Director, Office of Science, Office of Basic Energy Sciences, Materials Sciences Division, of the U.S. Department of Energy. The structural project on Photosystem I is supported by the National Science Foundation, grant number 0417142.

### **References.**

- David, W., Shankland, K., McCusker, L., Baerlocher, Ch. (2002). Structure determination from powder diffraction data. Oxford University Press. New York.
- DePonte, D.P. Weierstall, U. Starodub, D., Warner, J. Spence, J.C.H., Doak, R.B. J. Appl. Phys. (2008) in press.
- Henke, H., Gullikson, E., Davis, J. (1993) Atom. Data. Nucl. Data Tables **54**, 181-342.
- Howells, M.R., Beetz, T., Chapman, H.N., Cui, C. Holton, J.M., Jacobsen, C.J., Kirz, J., Lima, E., Marchesini, S., Miao, H., Sayre, D., Shapiro, D.A., Spence, J.C.H. (2008) J. Spectr. Rel. Phenom. In press.
- Jordan, P. Fromme, P., Witt, H.T., Klukas, O., Saenger, W., Krauss, N. (2001) Nature **411**, 909-917.
- Kisilak, M., Anderson, H., Babcock, N., Stetzer, M., Idziak, S. (2001) Rev Sci Instr. **72**, 4305-4307.
- Margiolaki, I. and Wright, J.P. (2008) Acta A64, in press.
- Neutze, R., Wouts, R., van der Spoel, D., Weckert, E., Hadju, J. (2000). Nature **406**, 752 - 757.
- Ourmazd, A., Shneerson, V. and Saldin, D.K. (2008) Acta **A64**, 303 - 315.
- Peterson, E., Buth, C., Arms, D. Dunford, R., Kanter, E., Krassig, B., Landahl, E., Pratt, S., Santra, R., Southworth, S., Young, L. (2008) Appl Phys. Letts. **92**, 094106.
- Rayleigh L (1878) On the Instability of Jets. Proc. London Math. Soc. 10: 4-13.
- Rasmussen SG, Choi HJ, Rosenbaum DM, Kobilka TS, Thian FS, Edwards PC, Burghammer M, Ratnala VR, Sanishvili R, Fischetti RF, Schertler GF, Weis WI, Kobilka BK (2007) Crystal structure of the human beta2 adrenergic G-protein-coupled receptor. Nature 450: 383-387

Shapiro, D. Thibault, P. Beetz, T., Elser, V., Howells, M., Jacobsen, C., Kirz, J., Lima, E., Miao, H., Neiman, A., Sayre, D. (2005) Proc. Nat. Acad. Sci. 102, 15343.  
Spence, J.C.H. and Doak, R.B. (2004) Phys. Rev. Letts. **92**, 198102.  
Starodub, D., Rez, P., Hembree, G., Howells, M., Shapiro, D., Chapman, H.N., Fromme, P., Schmidt, K. Weierstall, U. Doak, R.B., Spence, J.C.H. (2008) J. Synch. Rad. **15**, 62-73.  
Von Dreele, R.B. J. Appl. Cryst. (2007) **40**, 133-143  
Von Driel , R. Personal Communication (2007).  
Weierstall, U. , Doak, R.B., Spence, J.C.H., Starodub, D., Shapiro, D. Kennedy, P. Warner, J., Hembree, G.G., Fromme, P., Chapman, H. N. (2008) Exp. Fluids. In press.  
Wu, J. Weierstall, U., Spence, J. and Koch, C. (2004) Optics Letts. **29**, 1 -5.  
Wu, J., Leinenweber, K., Spence, J.C.H., O'Keeffe, M. (2006) Nature Materials **5**, 647 - 652.